Development of Ultraviolet Raman Diagnostics for Rocket Engine Injector Analysis

Joseph A. Wehrmeyer,* John M. Cramer,† Richard H. Eskridge,‡ and Chris C. Dobson§
NASA Marshall Space Flight Center, Huntsville, Alabama 35812

The development of a laser-based combustion diagnostics system and its application to the analysis of a high-pressure rocket engine injector flowfield are described. One dimensionally spatially resolved (linewise), multi-species, single-pulse images are obtained with an imaging spectrograph/digital camera detection setup that images spontaneous vibrational Raman light scattering caused by a pulsed ultraviolet laser, used to enhance Raman signal strength by the inverse fourth power of laser wavelength scaling for Raman scattering cross sections. These images provide temporally and spatially resolved qualitative information about the presence of gaseous major species (water vapor and molecular hydrogen, nitrogen, and oxygen) during a hot-fire, high-pressure (6.04-MPa) test of a single-element liquid oxygen/gaseous hydrogen swirled injector operating at a high oxidizer/fuel mixture ratio (100) in a test article pressurized by a nitrogen coflow. Raman images, taken every 40 ms, are generally uncorrelated with respect to each other during the constant pressure, main-stage portion of the test, but occasionally temporally adjacent image pairs are correlated, suggesting large-scale motion in the flow, possibly from transverse movements of the reactant jet within the diluent coflow. Simultaneous measurements of major species show unburnt ignitor gas (hydrogen) during the startup transient and excess diluent (nitrogen) during the shutdown transient, along with significant variations in the oxygen/nitrogen ratio during the test. Stimulated Raman and ozone production problems are investigated.

Introduction

LASER-BASED combustion diagnostics utilizing such techniques as spontaneous Raman scattering, coherent anti-stokes Raman scattering, or laser-induced fluorescence have been under development for decades and are now routinely applied in combustion experimentation.[1] Such applications are usually at or below atmospheric pressure, though high-pressure applications have been demonstrated for all three techniques.[2-4] When applied to rocket engine development, spectroscopy-based optical diagnostics encounter harsh conditions that include strong flame luminosity and very high pressure, enhancing line broadening, quenching, light trapping, and nonlinear optical activity.

Using gaseous hydrogen (GH$_2$) as the fuel and either liquid (LOX) or gaseous (GOX) oxygen as the oxidizer, hot-firing single-element rocket engine injector flows have been examined using spark shadowgraphy (LOX up to 10 MPa) (Ref. 5), Mie scattering (GOX or LOX up to 2.79 MPa) (Refs. 6 and 7), Doppler interferometry (GOX or LOX up to 2.79 MPa) (Refs. 8 and 9), laser-induced fluorescence (GOX at 1.31 MPa) (Ref. 9), predissociative laser-induced fluorescence (LOX up to 1 MPa) (Ref. 3) and spontaneous Raman scattering (GOX or LOX up to 6.89 MPa) (Refs. 4, 10, and 11). In addition, spontaneous Raman scattering has been applied in multi-element GH$_2$-fueled hot-fire flows (GOX up to 2.1 MPa) (Refs. 12 and 13). Of the single-element injector flows examined, all were for an axisymmetric, coaxial injector geometry with unswirled GH$_2$ as the annular flow, though the core flows were either unswirled (shear coaxial) GOX (Refs. 4, 6, 9, and 10) or LOX, (Refs. 3, 5, and 8) or swirled (swirl coaxial) GOX (Ref. 4) or LOX (Refs. 7 and 11).

These OX/GH$_2$ injector flowfields are of current interest in rocket engine design. Liquid/gas shear coaxial injectors are used in the space shuttle main engine's main chamber. Gas/gas coaxial injectors and liquid/gas swirled coaxial injectors are candidate injectors for advanced rocket engines employing the full flow staged combustion cycle,[14] with the former injector type used in the main chamber and the latter used in the oxidizer turbopump preburner, there providing combustion stability at high oxidizer/fuel (O/F) mixture ratios through improved atomization and mixing due to swirl.[15] Thus, gas/gas and liquid/gas mixing are key processes to investigate, especially for flows of extreme O/F ratios. Nonintrusive laser-based diagnostics can be used as part of this investigation.

Spontaneous Raman scattering, because it provides multispecies information, is an important laser-based technique to assess the mixing of molecularly disparate reactant streams. Additionally, the complete major species information of Raman can provide local chemistry, temperature, and pressure information.[16] Previous Raman work in rocket engines used either a flashlamp-pumped pulsed dye laser[4,10,13] or a frequency-doubled, pulsed, Nd-YAG laser[4,11,12] as the excitation source, both operating at visible wavelengths. Though adequate for low-pressure shear coaxial flows, the dye laser proved inappropriate for high-pressure, swirled flows whose higher background luminosity resulted in unacceptable interference during the long laser pulse (~ 3 μs) (Ref. 4). Background luminosity in such flows scales at least as the square of chamber pressure, though is relatively insensitive to O/F ratio.[5] To reduce detected background luminosity, the shorter pulse length (~ 7 ns) Nd-YAG laser was used, though, in general, these lasers have reduced pulse energy compared to flashlamp-pumped dye lasers.

The shorter Nd-YAG laser pulse allows shorter detection system gating periods to be used, resulting in less detected background luminosity. Thus, the detected background level (per unit of detector area) drops according to the ratio 3 μs/7 ns, or by a factor of ~ 400. To avoid photolytic processes at the sample volume, the Nd-YAG laser cannot be focused as tightly as the flashlamp-pumped dye laser. Spherical lenses, producing circular beam waists, are typically used for focusing of either laser. If the long pulse laser is focused just to the point of laser-induced breakdown, it can be expected that the short pulse laser beam waist will need to be larger in diameter than the long pulse by a ratio of the square root of the pulse length ratio, or square root (3 μs/7 ns) ~ 20 because photolysis depends

*NRC Senior Research Associate, Propulsion Laboratory; currently Research Associate Professor, Mechanical Engineering Department, Vanderbilt University, Box 1592 Station B, Nashville, TN 37235. Senior Member AIAA.
†System Engineer, Space Transportation Directorate. Senior Member AIAA.
‡Engineer, Space Transportation Directorate.
§Physicist, Space Transportation Directorate.

on laser intensity, which is inversely proportional to pulse duration and to beam waist area (which depends on the square of diameter). Because of its larger diameter and, hence, larger Raman image area, the short pulse laser beam will be decreased in signal strength (per unit of detector area) because its image is spread out over an area that is 20 times the area required to image the more tightly focused dye laser. Thus, the improvement in signal/background ratio going from the long pulse dye to short pulse Nd-YAG laser (assuming equal pulse energy) is 400/20, or a factor of 20.

In addition to photolysis, another consideration when using short pulse lasers is the production of stimulated Raman scattering in high-pressure rocket engines.[4,12] Pressure, path length, tightness of focus, and laser pulse energy all affect the production of stimulated Raman scattering, and, just as with photolysis, reduction of laser intensity can reduce stimulated Raman scattering. Multipulse time-averaged Raman signals[12,13] can be used to increase signal strength at the expense of losing instantaneous information, but such information may be critical when analyzing mixing processes that may include chemical reactions. Another way to increase signal strength is to use optical filters, rather than a less efficient spectrometer, to isolate spectrally a Raman signal,[4,10] but this generally does not allow single-pulse, simultaneous species data collection onto one imaging detector that provides spatial resolution in the detected Raman signals. Thus, further development of Raman systems for high-pressure rocket engine flows is desirable.

This paper addresses the need for improved high-pressure Raman systems by describing the development of high-pressure combustion diagnostics that utilize an ultraviolet (UV) light source. In particular, a narrowband, tunable (248–249 nm) krypton/fluoride excimer laser is used. By using a UV rather than a visible light source, the Raman scattering for a given laser pulse energy is increased by approximately the fourth power of the laser wavelength ratio.[16] Thus, the Raman scattered light produced by KrF excimer laser excitation is $(532/248)^4 \approx 21$ times that of a frequency-doubled Nd-YAG laser at equal pulse energy. By using optical components optimized for UV (e.g., blue enhanced intensifiers and UV-blazed gratings), the detection system efficiency for UV light can be similar to that for a visible Raman system. The increased signal strength of UV Raman allows for single-pulse measurements while using spectrometers coupled to array detectors for simultaneous, multispecies detection. The work described here uses an intensified charge-coupled device (CCD) digital camera coupled to an imaging spectrograph for single-pulse, multipoint (linewise), multispecies Raman measurements. This work's Raman data, though uncalibrated and, hence, unable to be used for absolute concentration and temperature measurements, nevertheless does provide insight into the flowfield of a swirled LOX/GH$_2$ injector flowfield operating at high pressure (6.04 MPa) by visualizing the movement of hot and cold flow regions (from the single-pulse, linewise nature of the measurements) and by showing instantaneous ratios of the major species Raman signals (exploiting the multispecies capability). Though providing more signal than visible excitation, UV Raman has the complications of fluorescence interference and possible ozone (O$_3$) production, with subsequent laser absorption by O$_3$. These issues are addressed and bounds on system configuration are determined for the successful application of UV Raman to high-pressure, oxygen-laden combustion environments.

Experimental

A Lambda-Physik COMPex 150T laser, with a nominal 0.001-nm linewidth and 50-Hz maximum repetition rate is used as the excitation source. Locking efficiency (percent of output within the tuned linewidth) is estimated to be better than 90%. The laser output is directed, using mirrors located in eye-safe ducting, out of a mobile instrumentation trailer down to the test article located outdoors. Figure 1 shows the experimental arrangement, which also includes an etalon/photodiode array assembly for real-time monitoring of laser locking efficiency. The path length is ~9 m from the laser to the test article. With a beam divergence of 0.2 mrad, this results in a 2-mm expansion of unfocused laser output, which has a nominal cross-sectional area of 1×2 cm. The test article consists
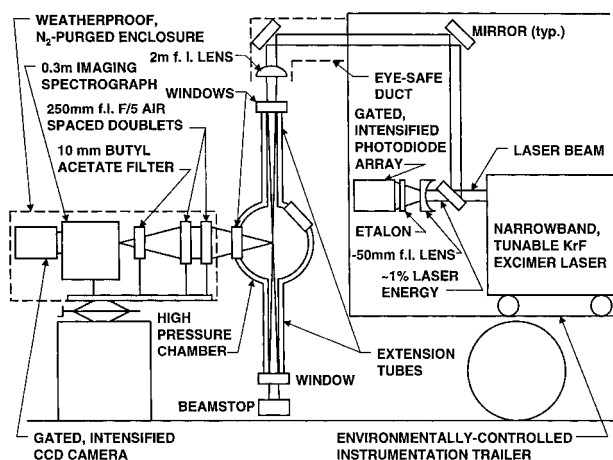

Fig. 1 Experimental system schematic for UV Raman system and high-pressure test article with extension tubes.
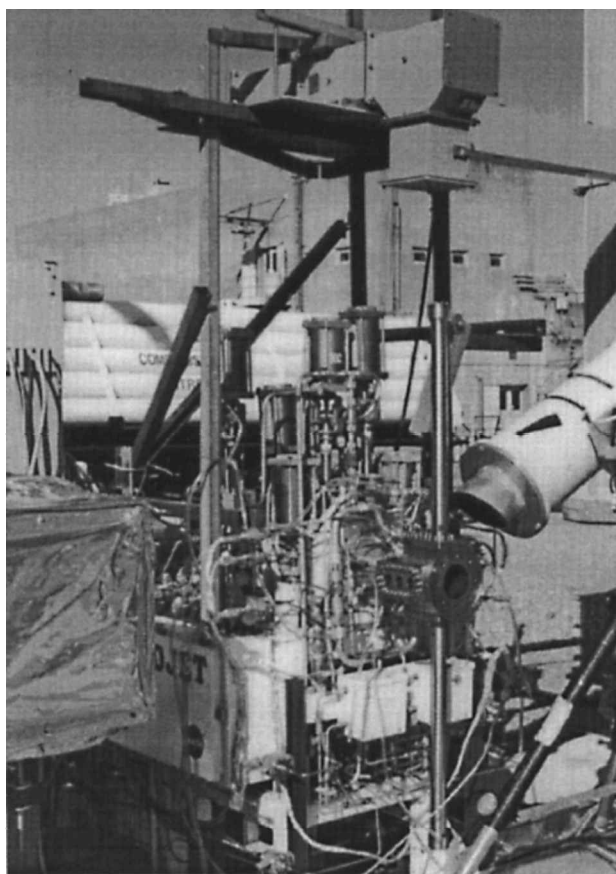

Fig. 2 Photograph of test article with throat plate removed.

of a windowed combustion chamber[17] within which is mounted a single-element swirled coaxial LOX/GH$_2$ injector, identical to one examined using other diagnostic techniques.[7] Figure 2 shows a photograph of the test article with the exit throat plate removed, showing the 8.7-cm-diam circular chamber. Figure 3 shows a side view schematic of the test article. The injector face is located 22.6 cm from the throat plane. The injector is mounted in a 3.0-cm-diam centerbody that extends 2.5 cm from the chamber head, which is actually a 2.5-cm annular injector containing a fine pattern of triplet elements, capable of providing a hot, reactive environment to be seen by the injector (see Ref. 17 for chamber details). Another thin annular flow at the chamber head periphery provides wall and window cooling. Table 1 lists the various flowrates for the oxygen-rich injector flowfield examined in this work. At these flowrates, the mean velocity expected in the test article is ~5 m/s.

Table 1 Parameters for single-element swirled LOX/GH₂ injector flowfield

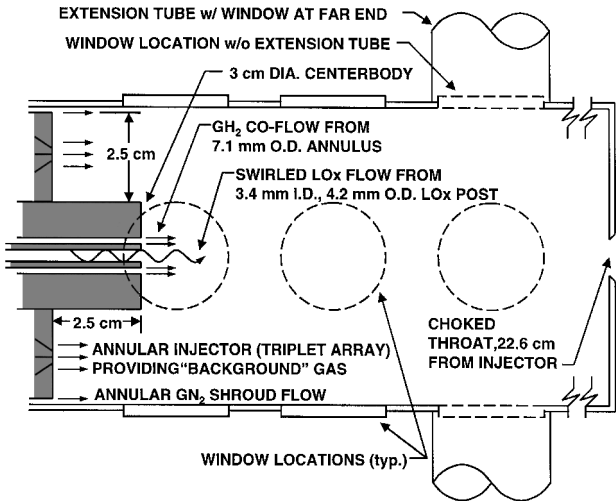| Parameter	Value
Chamber pressure, MPa	6.04
O/F ratio	100
Flowrates, kg/s	
LOX	0.1886
GH₂	0.00189
N₂ (annular injector and cooling circuits)	1.5

Fig. 3   Side view schematic of test article, showing extension tubes attached.

The laser beam propagates vertically through the chamber, entering at the top, exiting through the bottom, and terminating in a beam dump located outside the chamber. Optical access to the chamber is provided by 2.86-cm-diam windows mounted vertically and horizontally at three locations (1.1, 5.6, and 10.0 cm) downstream of the injector face. For good spatial resolution, it is desirable to focus the beam to a tight beam waist located near the centerline of the chamber. However, the resulting high laser fluence can cause problems of stimulated Raman and laser-induced breakdown in the chamber gases as well as possibly causing optical damage to the chamber windows. For some of the work described in this paper the laser beam was focused to a beam waist of ∼1 mm diameter (measured by inspection of optical damage on glass slides placed at focus) at the injector centerline using a 2-m lens. Extension tubes, shown in the schematic of Fig. 1 and appearing in the photograph of Fig. 2 both above and below the test article, were used to extend the windows from the beam waist. The design criterion for placement of the windows (68.6 cm from injector centerline and beam waist) was to subject them to a fluence of 2 J/cm², a level that when exceeded can cause single-pulse color center production in certain types of fused silica.[18] Color center production in fused silica, either by single-pulse or multipulse processes, is to be avoided because it gradually decreases the UV transmission of the material. Corning 7940 fused silica was the chosen window material and multipulse damage (several thousand pulses) did occur. Suprasil 312 could be a material more resistant to multipulse damage.

Scattered light was collected at 90 deg to the laser beam using an F/5 fused silica air-spaced doublet. Another identical lens focused the collected light into a 0.3-m imaging spectrograph. The long dimension of the entrance slit was vertically aligned with the laser beam image so that the vertical dimension of the CCD provided spatially resolved data for an 8.4-mm laser beam length that is located near the injector centerline. The hot-fire data of this paper are obtained at the 10.0-cm axial location. Spectral information is provided by the horizontal CCD dimension (12.7 mm), which, when coupled with a 1200 groove/mm grating, provides a 34-nm range, sufficient to simultaneously image the Rayleigh signal and the four

major species Raman signals (O₂, 259; N₂ 264; H₂O, 274; and H₂, 277 nm). The CCD camera has an intensifier gated at 50 ns to suppress detected background luminosity.

Stimulated Raman Scattering

Because stimulated Raman scattering has been a problem in past applications of pulsed lasers for high-pressure Raman gas diagnostics,[4,12] the range of operating conditions over which spontaneous Raman occurs was determined for the present system. The combustion chamber's exit throat was sealed, and N₂ at ∼10°C was introduced into the chamber at various pressures. The amount of incident laser energy that is Raman shifted depends nonlinearly on gas pressure, laser pulse energy, and path length.[19] With the path length set at 68.6 cm (from the upstream beginning of the high-pressure region down to the sample volume location) both the pressure and pulse energy were varied. Figure 4 shows six consecutive single-pulse N₂ Raman signals for three different pressure/pulse energy combinations. The a–f spectra of Fig. 4 are for 310 mJ/pulse and 3.54 MPa (35 atm). Both the signal strength and spectral shape are the same among these spectra. Increasing the pulse energy to 400 mJ causes the intermittent production of stimulated Raman in some pulses (g–l in Fig. 4) with a portion of this coherent, directed light subsequently elastically scattered and detected away from the laser beam axis. The detected Raman signal is no longer consistently linearly related to laser pulse energy. Because of the nonlinearity of the stimulated Raman process, small variations in the distribution of laser intensity across the beam area result in large variations in pulse-to-pulse detected Raman signal. Increasing the pressure up to 69 atm while keeping the pulse energy constant at 400 mJ results in stimulated Raman production with every laser pulse (m–r in Fig. 4). Table 2 lists the pressure/pulse energy combinations for which stimulated Raman scattering either intermittently or always occurs.

Table 2 Range of pressures and pulse energies for spontaneous or stimulated Raman[a]

Pressure, atm	Pulse energy, mJ		
	210	310	400
1	SP	SP	SP
18	SP	SP	SP
35	SP	SP	INT
69	INT	ST	ST
100	ST	ST	ST

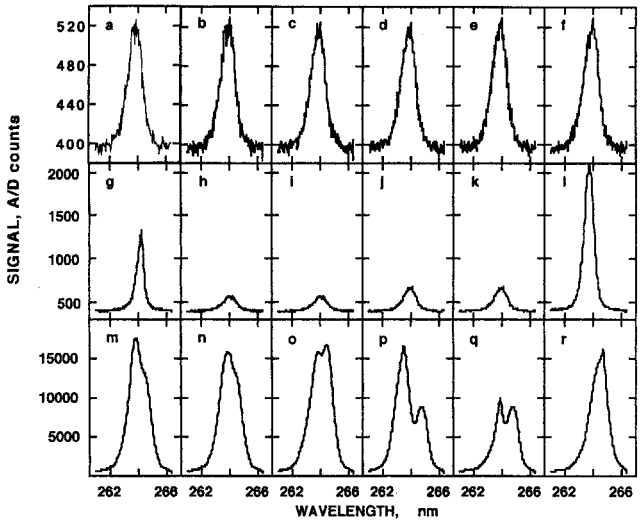[a]SP, spontaneous; ST, stimulated; INT, intermittent spontaneous or stimulated.

Fig. 4   Three sets of consecutive single-pulse N₂ stokes vibrational Raman signals: a–f, 310 mJ/pulse, 35 atm; g–l, 400 mJ/pulse, 35 atm; and m–r, 400 mJ/pulse, 69 atm.
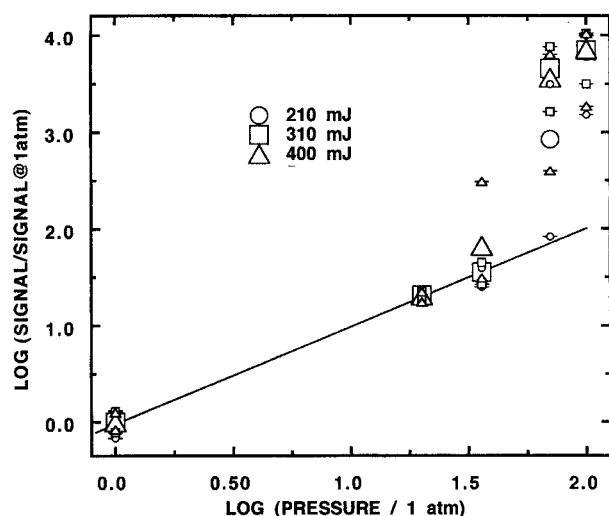
Fig. 5 Log of N_2 stokes vibrational Raman signal (normalized by signal at 1 atm) vs log of pressure (normalized by 1 atm) for three pulse energies; system using extensions and focused laser (large data points average of 100 pulse sample, small data points maximum and minimum of each sample).

Figure 5 shows average values of detected N_2 stokes Raman signal (normalized by the Raman signal at 1 atm for the corresponding pulse energy) as a function of pressure ranging from 1 to 100 atm, and pulse energy ranging from 210 to 400 mJ (2.7×10^4 to 5.1×10^4 mJ/cm^2 fluence at beam waist). Maximum and minimum signal strengths for each 100-shot sample are represented by smaller symbols in Fig. 5. Linearity of the Raman signal with respect to pressure and pulse energy is demonstrated at the lowest two pressures for all three pulse energies. Relatively little scatter in single-pulse data is also seen at these pressures with the maximum and minimum values lying close to average values for each data set. However, at 35 atm the intermittent production of stimulated Raman for 400-mJ pulses cause the average value of that data set to lie above the linear curve and the maximum value is almost one order of magnitude greater than that set's average value. Further increases in pressure cause the average values to deviate even further (about two orders of magnitude) from linearity with respect to pressure, although at 69 atm and 210 mJ/pulse the intermittent absence of stimulated Raman allows the minimum value for that data set to lie near the linear curve. Thus, the maximum pressure for which the Raman system, with a focused beam and extension tubes, can provide data linear with respect to pulse energy and species number density is approximately 35 atm. Higher temperatures with lower number density at hot-fire conditions may raise this pressure limit, but ambient temperature calibrations at high pressures[4,10–13] are still needed to transform Raman data into concentration measurements.

UV Photolytic and Fluorescence Processes

UV Raman, although providing more Raman signal than visible Raman for a given pulse energy (assuming similar sensitivities for UV and visible Raman detection systems), has the potential to cause photolytic or fluorescent interferences. Broadband (248–249 nm bandwidth) KrF lasers have been shown to cause significant OH and O_2 fluorescence in atmospheric-pressure flames, but narrowband, tunable lasers greatly reduce the interference when tuned away from molecular transitions.[20] As pressure increases, however, the molecular transitions' collision linewidths increase so that the laser cannot be tuned to completely avoid fluorescence excitation. To predict the influence of pressure on OH excitation, the linewidth of the OH transitions accessed by the KrF laser were modeled. Figure 6 shows the theoretical pressure effect on the OH A $\leftarrow$ X (3, 0) transitions accessible by the KrF excimer laser. Collision linewidths are estimated using data for (1, 0) transitions[21] and are 0.08, 4, and 8 cm^{-1} for pressures of 1, 50, and 100 atm, respectively. The Doppler width is modeled at 0.3 cm^{-1} for all pressures. If fluores-
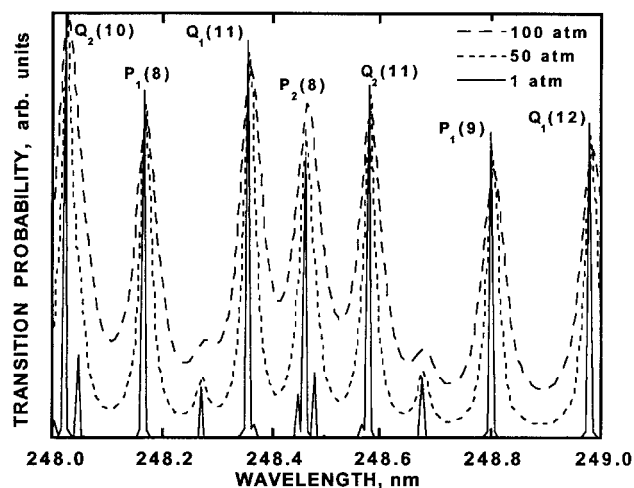

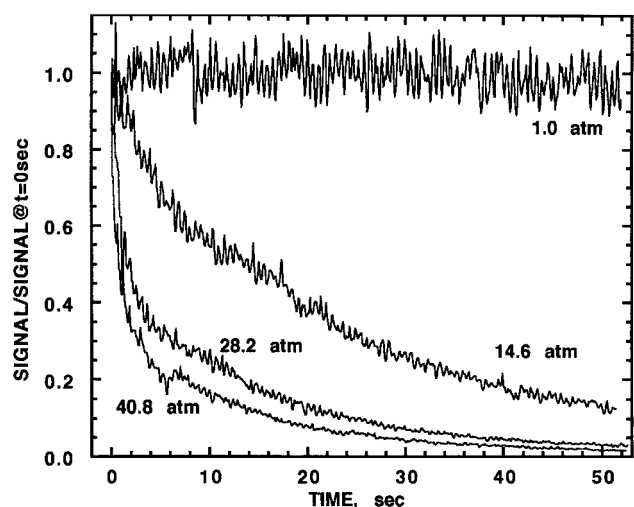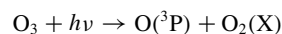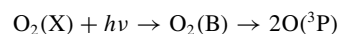**Fig. 6   Calculated OH transitions near 248.5 nm for three pressures.**

Fig. 7 N_2 stokes vibrational Raman signal vs time for air-filled chamber (with extensions) at various pressures and for broadband excitation.

cence interference is problematic, the unpolarized fluorescence can be removed from polarized Raman signals by using polarized signal detection techniques.[22]
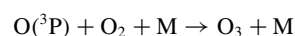
Another important UV process is the photolytic production of O_3. Ozone has a large absorption cross section at 248 nm and, if present, can greatly attenuate laser energy delivered to the measurement sample volume. Production of O_3 from irradiation of 1000-torr O_2 with a tunable KrF laser has been demonstrated,[23] even though 248-nm radiation is not energetic enough to directly dissociate ground-state O_2. The production mechanism is the initial photodissociation of trace amounts of nascent O_3 into O(^{3}P) and vibrationally excited O_2(X), which in turn is then photodissociated into two O atoms via the high predissociation rate of O_2(B) after exciting O_2(X) to O_2(B). Here the symbols in parentheses represent the electronic states of the atoms and molecules. Each of the three resulting O atoms combines with an O_2 molecule in the presence of a third body M to form O_3. Thus, three O_3 molecules are created from a single O_3 molecule photodissociating through two separate single-photon processes. The sequence is step 1,

$$O_3 + h\nu \rightarrow O(^3P) + O_2(X)$$

step 2,

$$O_2(X) + h\nu \rightarrow O_2(B) \rightarrow 2O(^3P)$$
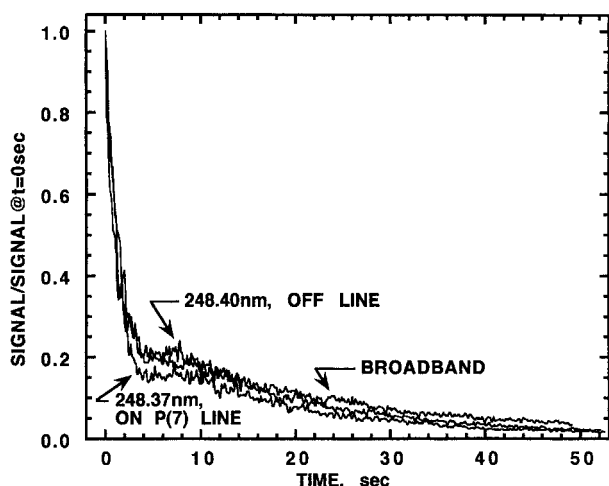
and step 3,

$$O(^3P) + O_2 + M \rightarrow O_3 + M$$

Fig. 8 N₂ stokes vibrational Raman signal vs time for air-filled chamber (with extensions) at 40.8 atm and for three laser linewidth/tuning combinations: narrowband at 248.40 or 248.37 nm, or broadband.

Fig. 9 Log of N₂ stokes vibrational Raman signal (normalized by signal at 1 atm) vs log of pressure (normalized by 1 atm) for three pulse energies; system uses unfocused beam without extensions.

Because the last O_3 production step involves a third body, and the major O_3 destruction rates involve two-body collisions only,[24] the overall production rate of O_3 increases with pressure. To determine the effect of 248-nm O_3 production at high pressure, the sealed chamber, with extensions, was filled with air at various pressures and the single-pulse, time-varying Raman signal was measured. Figure 7 shows the N_2 stokes vibrational Raman signal (normalized by the first pulse's signal for each of the four data sets) as a function of time (10-Hz laser repetition rate, broadband laser). At 1 atm the measured N_2 Raman signal remains relatively constant with time, with random fluctuations caused by pulse-to-pulse variations in laser energy. However, at 14.6 atm the measured signal decreases with time (as does the amount of laser energy exiting the chamber) due to O_3 absorption. The rate of signal decrease is even more pronounced at 28.2 and 40.8 atm.

Operating the laser in the narrowband mode and tuning between O_2 (B ← X) transitions has been shown to influence the rate of O_3 production at ~1 atm (Ref. 23), but little influence of laser tuning on the O_3 production rate occurs when operating at 40.8 atm (see Fig. 8). Tuning onto a particular excitation line, the (2, 7) P(7), results in a slightly higher rate of signal reduction compared to tuning away from that transition. The signal reduction for broadband laser excitation generally lies between that for the narrowband laser operating either on an O_2 absorption line or away from an O_2 absorption line, but differences among the three data sets are slight. This insensitivity to tuning must be due in part to the broadening of the O_2 transitions (for the O_2 photodissociation of step 2) with increased pressure.

Because the extension tubes that separate the laser windows from the beam waist are unpurged, they have the potential for harboring unreacted O_2 during a hot-fire test. The resulting O_3 production and subsequent beam attenuation provide a severe challenge to providing a Raman system calibration (necessary for quantitative measurements) that is good for the test duration. This, when coupled with the propensity for stimulated Raman to occur down the length of the upper extension tube at high pressure, indicates that unpurged extension tubes should not be used when applying UV Raman to high pressure. For all subsequent data, the extension tubes are removed, forcing the laser to remain unfocused through the combustion chamber to avoid window damage. Coarsened spatial resolution is the tradeoff, though flow structure can still be seen in the hot-fire data of the following section.

Figure 9 shows the N_2 stokes vibrational Raman signal strength (normalized by signal strength at 1 atm for the corresponding pulse energy) for the new configuration. Linearity between signal and pressure is generally observed for this ambient temperature data at all pressures and pulse energies due to the absence of stimulated Raman. Ozone production will still occur and attenuate the laser
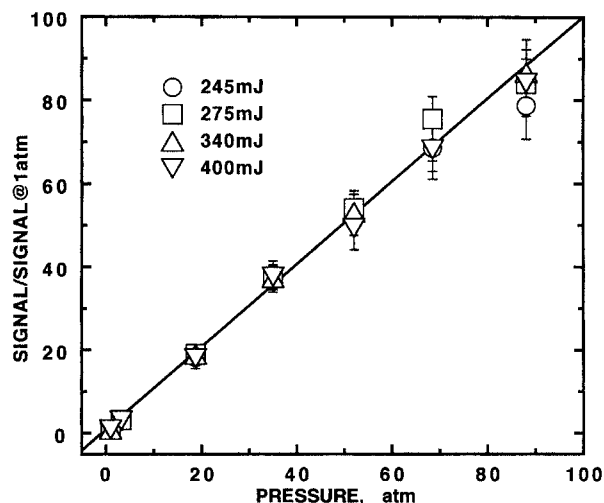
energy and Raman signal, but only over the 4.3-cm radius of the chamber instead of the 68.6-cm path length provided by the extension tubes. Inside the chamber, the beam path is continually swept by fresh gas during a test so that O_3 produced after a laser pulse will be swept out before the next pulse.

Single-Pulse Raman Images for Hot-Fire Conditions

With extension tubes absent and using an unfocused laser beam, single-pulse Raman images are obtained in a hot-fire environment. Specifically, the reacting flowfield produced by a swirled LOX/GH₂ injector is examined, a flowfield whose atomization characteristics have already been investigated.[7] Table 1 lists the flowfield conditions. Measurements are obtained from the window set located farthest downstream (10.0 cm from injector face) and near the chamber centerline. The 8.4-mm spatial dimension of the CCD is binned into 12 strips, each associated with 0.7 mm of sampled laser beam length. The spatial resolution for each measurement location is 1.2 mm (determined by the spectrograph slit width) down the injector/chamber centerline, 20 mm (determined by laser beam cross section) down the optical detection system axis, and approximately 1.7 mm (determined by CCD binning and by the detection system's depth-of-field coupled with laser beam cross section) down the laser axis. The UV Raman system was operated at 25 Hz.

A typical test run lasts for approximately 20 s with 10 s at steady state. Figure 10 shows the chamber pressure P_c rising from its 0.86 MPa (124 psia) start condition (N₂ purges on before start) up to a steady-state pressure of 6.04 MPa (875 psia) (with propellant flows at full values and the annular circuit providing additional GN₂ flow to achieve desired pressure). During pressure ramp up a GH₂–GO₂ ignitor torch fires to ignite the injector propellants, and at 4.74 s the torch is purged with GN₂, resulting in a sudden burst of rich, unreacted gas into the chamber with a concomitant spike in P_c. The Raman image for this specific time (shown in upper left of Fig. 10) shows unreacted H₂ in the chamber (shown by its 277-nm Raman signal), and high signal strength for all species indicates low-temperature, high-density conditions.

Typical Raman images obtained during steady state are shown on the right of Fig. 10. These are four consecutive images, taken at 40-ms intervals (25 Hz), the time interval between consecutive laser pulses. The top right graph in Fig. 10 shows typical signal strengths during the test. The next image down, obtained 40 ms later, shows an increase in the Raman signal intensity, especially for the N₂ signal. The third graph on the right of Fig. 10 still shows relatively strong Raman signals, but the position of the maximum signal has moved from 8.4 mm to the 0.0 mm location, showing movement (of the region producing high Raman signals) transverse to the chamber/injector centerline. The next consecutive Raman image at the
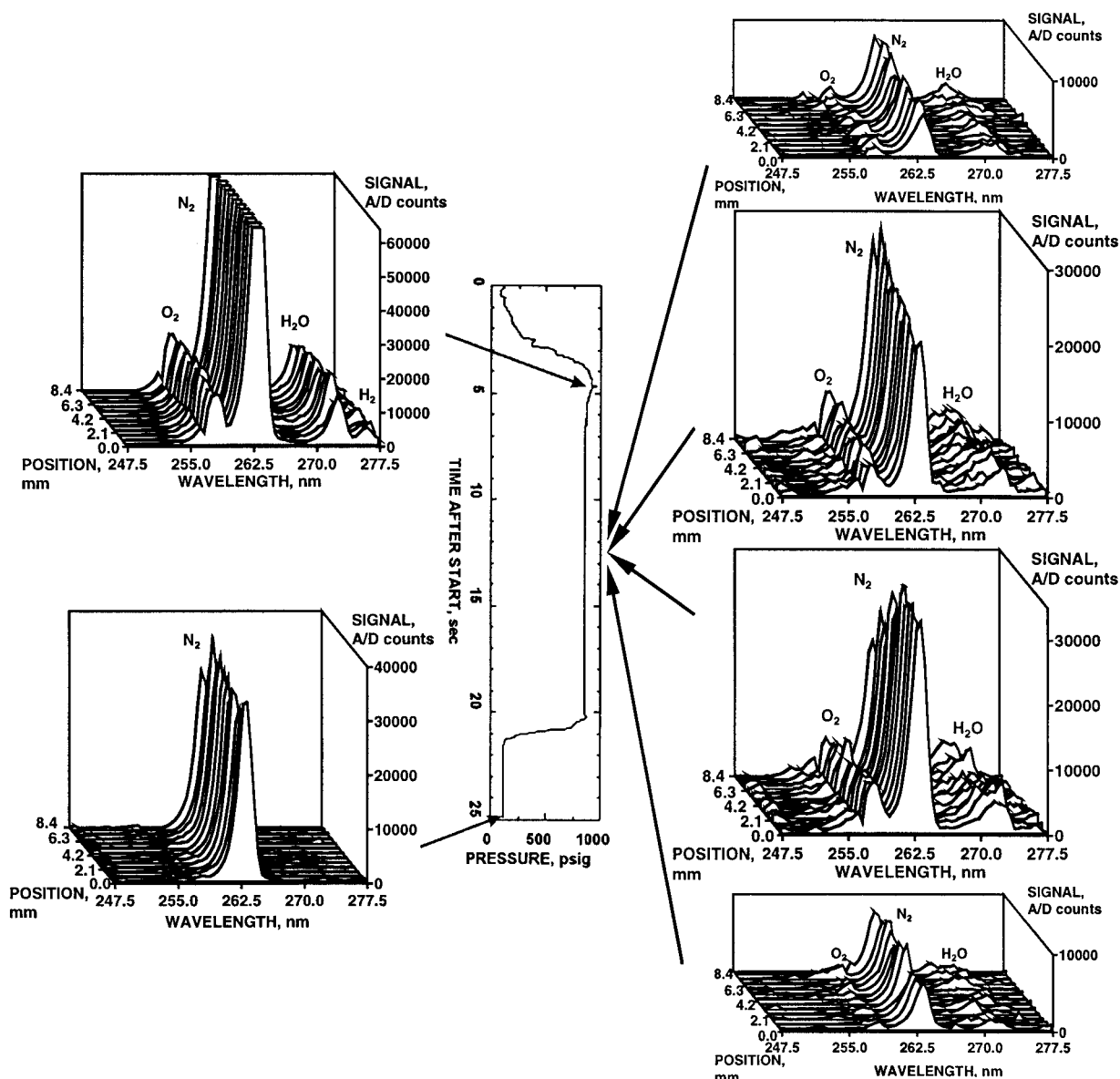
Fig. 10   Spatially resolved, single-pulse Raman images for oxygen-rich swirled injector hot-fire test, 6.04 MPa (875 psia).

bottom right of Fig. 10 shows the Raman signals returning to normal, low values. In all of the four consecutive Raman images, there can be seen the O_2, N_2, and H_2O Raman signals, indicating considerable mixing has occurred at this downstream location between the injector propellants and the annular GN_2 flow. The pressure trace shown in Fig. 10 was obtained from a high-frequency-response pressure transducer and shows no large pressure fluctuations in the chamber pressure during its main-stage operation. Thus, the increase in Raman signal for the middle two Raman images is not due to a pressure transient that would momentarily increase density and, hence, Raman signal strength. However, this phenomenon of temporally adjacent Raman images being correlated to each other occurs fairly often during the test, suggesting that there is some kind of pressure-independent density fluctuation occurring at a relatively large temporal scale ($\sim$40 ms). This temporal scale seems too large for turbulent fluctuations. The average velocity in the test chamber is $\sim$5 m/s; within 40 ms the flow has traveled an average of 20 cm, a length too long to be associated with a turbulent eddy size. Possible explanations for the temporal correlation between the middle two Raman images include the movement of large-scale coherent structures through the sample volume and flapping of the center jet of products/reactants within the N_2 diluent coflow, resulting in Raman images that are intermittently taken within the center jet and

at other times either partially or completely outside the jet. After the propellant flows are shut down, the only specie remaining in the chamber is N_2, as seen in the bottom left graph on Fig. 10.

None of the single-pulse Raman images obtained during the test showed any significant OH or O_2 fluorescence interference. This is because the temperatures in the test article are generally below 1000 K, due to the high O/F ratio of the reactants and the relatively large amount of N_2 dilution occurring in the flow. Because of the low temperatures, the concentration of OH outside of the flame zones is very low, and the fraction of O_2 that is vibrationally excited is also very low. Because only vibrationally excited O_2 can be excited by a 248-nm laser,[20] neither OH nor O_2 fluorescence occurs in this particular flowfield.

The wavelength-integrated Raman signal for each major species is shown in Fig. 11 as a function of time. These data are for one location of the 12 separate locations measured by the detection system. Large fluctuations in signal strength occur for all three species, caused by both local temperature (density) fluctuations and by fluctuations in the local gas mix. This latter fluctuation can be demonstrated in the ratio of one Raman signal to another. Figure 11e shows relatively large fluctuations in the O_2/N_2 ratio, indicating incomplete mixing between the injector and annular streams. As the propellant circuits are purged during shutdown, the O_2/N_2 ratio rises dramatically,
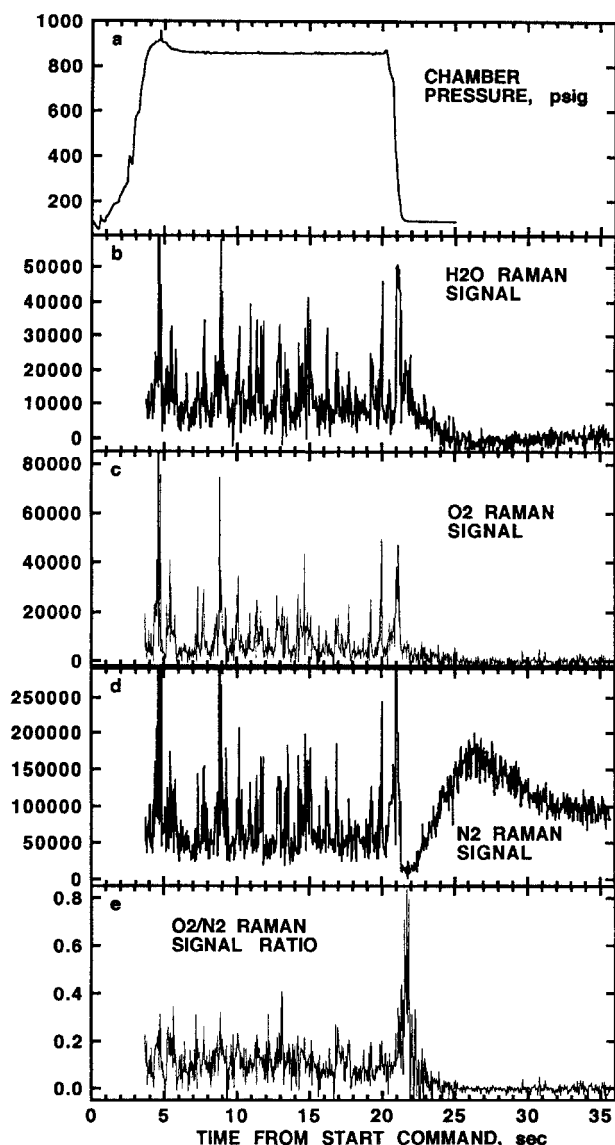
Fig. 11 Time-resolved data from hot-fire test of oxygen-rich swirled injector, steady-state pressure 6.04 MPa (874.7 psia); Raman signals are wavelength integrated and are expressed in A/D counts.

Raman data. Fluctuations in relative concentrations are seen during the steady-state portion of the test, and often during the test these fluctuations can be correlated between single-pulse images taken at 40 ms intervals. This timescale is too large for turbulence to cause the fluctuations, and test article chamber pressure remains constant during main-stage operation. The fluctuations in Raman signal could be due to intermittant sampling of the propellant stream and the coannular diluent flow surrounding it. Significant deviations from steady state are seen in the reactant concentrations at the test transients, such as the presence of unreacted H_2 at startup or excess O_2 at shutdown. Future investigations will include an experimental calibration to transform the Raman measurements into absolute concentration and temperature measurements.

UV Raman scattering has been applied to the analysis of a high-pressure reacting flow such as those found in liquid-fueled rocket engines. The UV wavelength of a KrF laser produces over an order of magnitude more Raman scattering than a visible laser of comparable pulse energy, but with the extra signal strength comes concerns about the UV system's applicability to quiescent O_2 flows (because of O_3 production and subsequent laser absorption). The O_3 production trait of high-pressure UV Raman scattering generally precludes the use of unpurged laser window extension tubes, where O_2 can be trapped and then form absorptive O_3. By purging the laser window extension tubes with a diluent, it could be possible to avoid O_3 production, and then a tightly focused UV laser beam could be created in the test article. As long as the test article has a moving stream of reactants, the small amount of O_3 generated within the test article, for each single laser pulse, is swept downstream out of the laser beam path, and significant laser beam attenuation should not occur. To avoid the interfering effects of stimulated Raman scattering, the diluent used to purge the extension tubes should be helium because of its small scattering cross sections.

Temperatures in the N_2-diluted, high O/F ratio flowfield examined are generally below 1000 K; thus, OH and O_2 fluorescence were not a major concern. However, as the UV Raman system is applied to higher temperature flowfields (near stoichiometric and/or less dilute), the increased collisional broadening of excitation lines at high pressure may produce significant fluorescence interference of Raman signals. This could be a potential limitation to the applicability of the UV Raman technique applied to high-pressure rocket engine flows. Polarization separation techniques are being developed that address this potential problem so that the increased signal strength provided by UV Raman can be exploited in H_2/O_2 rocket engines of all stoichiometries and possibly in soot-free regions of RP1/O_2 engines.[22]

Acknowledgments

probably due to the fuel circuit shutdown occurring 0.45 s before oxidizer circuit shutdown, allowing unreacted O_2 to exist in larger concentrations than at steady state.

Conclusions and Future Work

The production of O_3 by the KrF excimer laser has been shown to cause time-dependent absorption of the laser beam as it propagates through the combustion chamber and extension tubes. Absorption increases with pressure, and at realistic rocket engine operational pressures this phenomenon prohibits the use of unpurged extension tubes where quiescent O_2 may accumulate. Additionally, stimulated Raman occurs for focused laser beams that require the extension tubes (to lower laser fluence level experienced by windows) so that the final Raman system configuration uses an unfocused laser beam without combustion chamber extension tubes. The resulting spatial resolution is approximately $1.7 \times 1.2 \times 20$ mm for single-pulse, linewise (12 spatial locations in 8.4 mm) measurements. Future improvements to the system include aperturing the unfocused laser beam to a 1-mm-diam cross section to improve spatial resolution while avoiding high fluence.

An O_2-rich swirled injector flowfield is examined with the UV Raman system. The presence and relative concentration of a particular major species during the test can be determined from the

References

[1]Eckbreth, A. C., *Laser Diagnostics for Combustion Temperature and Species*, edited by A. K. Gupta and D. G. Lilley, Energy and Engineering Science Series, Vol. 7, Abacus, Cambridge, MA, 1988.

[2]Bergmann, V., and Stricker, W., "H_2 CARS Thermometry in a Fuel-Rich, Premixed, Laminar CH_4/Air Flame in the Pressure Range Between 5 and 40 Bar," *Applied Physics B*, Vol. 61, No. 1, 1995, pp. 49–57.

[3]Brummond, U., Cessou, A., and Vogel, A., "PLIF Imaging Measurements of a Coaxial Rocket Injector Spray at Elevated Pressure," *Proceedings of the 26th Symposium (International) on Combustion*, Combustion Inst., Pittsburgh, PA, 1996, pp. 1687–1695.

[4]Foust, M. J., Pal, S., and Santoro, R. J., "Gaseous Propellant Rocket Studies Using Raman Spectroscopy," AIAA Paper 96-2766, July 1996.

[5]Mayer, W., Schik, A., Schweitzer, C., and Schaffler, M., "Injection and Mixing Processes in High Pressure LOX/GH_2 Rocket Combustors," AIAA Paper 96-2620, July 1996.

[6]Moser, M. D., Pal, S., and Santoro, R. J., "Laser Light Scattering Measurements in a GO_2/GH_2 Uni-Element Rocket Chamber," AIAA Paper 95-0137, July 1995.

[7]Rahman, S. A., Pal, S., and Santoro, R. J., "Swirl Coaxial Atomization:

Cold-Flow and Hot-Fire Experiments," AIAA Paper 95-0381, Jan. 1995.

[8]Pal, S., Moser, M. D., Ryan, H. M., Foust, M. J., and Santoro, R. J., "Flowfield Characteristics in a Liquid Propellant Rocket," AIAA Paper 93-1882, June 1993.

[9]Moser, M. D., Merenich, J. J., Pal, S., and Santoro, R. J., "OH-Radical Imaging and Velocity Field Measurements in a Gaseous Hydrogen/Oxygen Rocket," AIAA Paper 93-2036, June 1993.

[10]Foust, M. J., Deshpande, M., Pal, S., Ni, T., Merkle, C. L., and Santoro, R. J., "Experimental and Analytical Characterization of a Shear Coaxial Combusting GO_2/GH_2 Flowfield," AIAA Paper 96-0646, Jan. 1996.

[11]Yeralan, S., Pal, S., and Santoro, R. J., "Major Species and Temperature Profiles of LOX/GH_2 Combustion," AIAA Paper 97-2940, July 1997.

[12]Farhangi, S., Gylys, V. T., and Jensen, R. J., "Gas Composition and Temperature Measurements in a Rocket Engine Combustor Using the Raman Technique," AIAA Paper 94-0225, Jan. 1994.

[13]Jones, R. A., de Groot, W. A., Myrabo, L. N., and Nagamatsu, H. T., "Oxygen Temperature and Concentration Measurements in H_2–O_2 Rocket Engines," AIAA Paper 96-0439, Jan. 1996.

[14]Knuth, W. H., and Crawford, R. A., "Oxygen-Rich Combustion Process Applications and Benefits," AIAA Paper 91-2042, June 1991.

[15]*Liquid Rocket Engine Injectors*, NASA SP-8089, 1976.

[16]Cheng, T. S., Wehrmeyer, J. A., Pitz, R. W., Jarrett, O., Jr., and Northam, G. B., "Raman Measurements of Mixing and Finite-Rate Chemistry in a Supersonic H_2-air Diffusion Flame," *Combustion and Flame*, Vol. 99, No. 1, 1994, pp. 157–173.

[17]Hulka, J., and Makel, D., "Liquid O_2/H_2 Testing of a Single Swirl Coaxial Injector Element in a Windowed Combustion Chamber," AIAA Paper 93-1954, 1993.

[18]Lowdermilk, W. H., and Milam, D., "Review of Ultraviolet Damage Threshold Measurements at Lawrence Livermore National Laboratory," *(SPIE) Society of Photo-optical Instrumentation Engineers Vol. 476, Excimer Lasers, Their Applications, and New Frontiers in Lasers*, Society of Photo-Optical Instrumentation Engineers, Bellingham, WA, 1984, pp. 143–162.

[19]White, J. C., "Stimulated Raman Scattering," *Tunable Lasers, Topics in Applied Physics*, Vol. 59, Springer-Verlag, Berlin, 1987, pp. 115–207.

[20]Wehrmeyer, J. A., Cheng, T. S., and Pitz, R. W., "Raman Scattering Measurements in Flames using a Tunable KrF Excimer Laser," *Applied Optics*, Vol. 31, No. 10, 1992, pp. 1495–1504.

[21]Kessler, W. J., Allen, M. G., and Davis, S. J., "Rotational Level-Dependent Collisional Broadening and Line Shift of the $A^2\Sigma^+$-$X^2\Pi(1, 0)$ Band of OH in Hydrogen–Air Combustion Gases," *Journal Quantitative Spectroscopy Radiation Transfer*, Vol. 49, No. 2, 1993, pp. 107–117.

[22]Hartfield, R. J., Jr., Dobson, C. C., Eskridge, R. H., and Wehrmeyer, J. A., "Development of a Technique for Separating Raman Scattering Signals from Background Emission with Single-Shot Measurement Potential," AIAA Paper 97-3357, 1997.

[23]Slanger, T. G., Jusinski, L. E., Black, G., and Gadd, G. E., "A New Laboratory Source of Ozone and its Potential Atmospheric Implications," *Science*, Vol. 241, No. 4868, 1988, pp. 945–950.

[24]Freisinger, B., Kogelschatz, U., Schafer, J. H., Uhlenbusch, J., and Viol, W., "Ozone Production in Oxygen by Means of F_2-Laser Irradiation at $\lambda = 157.6$ nm," *Applied Physics B*, Vol. 49, No. 2, 1989, pp. 121–129.